Remote Sens. **2013**, *5*, 6958-6975; doi:10.3390/rs5126958

OPEN ACCESS

Remote Sensing

ISSN 2072-4292

www.mdpi.com/journal/remotesensing

Article

The Application of Deep Convective Clouds in the Calibration and Response Monitoring of the Reflective Solar Bands of FY-3A/MERSI (Medium Resolution Spectral Imager)

Lin Chen [1,2,*], Xiuqing Hu [1,2], Na Xu [1,2] and Peng Zhang [1,2]

[1] Key Laboratory of Radiometric Calibration and Validation for Environmental Satellites, China Meteorological Administration (LRCVES/CMA), No. 46 Zhongguancun Nandajie Rd., Beijing 10081, China; E-Mails: huxq@cma.gov.cn (X.H.); xuna@cma.gov.cn (N.X.); zhangp@cma.gov.cn (P.Z.)

[2] National Satellite Meteorology Center, China Meteorological Administration (NSMC/CMA), Beijing 100081, China

* Author to whom correspondence should be addressed; E-Mail: chenlin@cma.gov.cn; Tel.: +86-10-6840-6704.

Received: 7 October 2013; in revised form: 14 November 2013 / Accepted: 18 November 2013 / Published: 12 December 2013

Abstract: Based on simulated reflectance, deep convective clouds (DCC) can be used as an invariant target to monitor the radiometric response degradation of the FY-3A/MERSI (Medium Resolution Spectral Imager) reflective solar bands (RSBs). The long-term response of the MERSI RSBs can easily be predicted using a quadratic fit of the monthly DCC mean reflectance, except for bands 6 and 7, which suffer from instrument anomalies. DCC-based degradations show that the blue bands ($\lambda < 500$ nm) and water-vapor bands have degraded significantly, whereas for near-infrared bands, the total degradations in four years are within 3% (excluding bands 3 and 20). For most bands, the degradation rates are greatest during the first year in orbit and decrease over time. The FY-3A/MERSI degradation results derived from DCC are consistent within 2.5%, except for bands, 11, 18 and 19, when compared with Aqua/MODIS(Moderate Resolution Imaging Sepetroradiometer) inter-calibration, multi-site invariant earth target calibration and the CRCS(Chinese Radiometric Calibration Site) Dunhuang desert vicarious calibration methods. Overall, the 2σ/mean degradation uncertainty for most MERSI bands was within 3%, validating the temporal stability of the DCC monthly mean reflectances. The DCC method has reduced the degradation uncertainties for MERSI water vapor bands over other methods. This is a

significant advantage of the DCC calibration method. The saturation of some MERSI bands may hinder the effectiveness of the DCC calibration approach.

Keywords: deep convective cloud; radiometric calibration; response degradation; MERSI; reflective solar bands

1. Introduction

Considering that some space-borne instruments do not carry onboard calibration devices for reflective solar bands (RSBs) or even if they do, these devices, when exposed to the space environment and high energy solar radiation, usually may be subject to deterioration. Therefore, it is required to update the calibration coefficient frequently by all kinds of means of in-flight vicarious calibration (VC). Based on whether the vicarious calibration is conducted on the ground test site or not, the VC calibration can be divided into site-based calibration and non-site-based calibration [1–3]. Since site-based calibration often costs a large amount of human and financial resources and the frequency of calibration is also limited, it is difficult to conduct re-calibration for the historical data. Non-site-based VC calibration without ground reflectance and atmospheric measurements performed simultaneously with the satellite overpass started in the 1990s. Currently, the calibration coefficient is often obtained by several vicarious calibrations after launch. These methods include stable desert target, snow ice, synchronous in-flight calibration and the inter-calibration using other sensors with high accuracy calibration [4–9].

Due to the need for long-term monitoring of climate change, upon the proposal of NOAA/NESDIS (National Oceanic and Atmospheric Administration, National Environmental Satellite Data and Information Service), WMO (World Meteorological Organization) and CGMs (Coordination Group for Meteorological Satellites) approved the decision to build a global space-based inter-calibration system in 2005 to serve the end of promoting the research of absolute radiometric calibration of a satellite sensor [10,11]. In recent years, to ensure the accuracy of satellite data, testing on the radiometric calibration precision of remote sensors has become an urgent task facing the world's scientists for remote sensing. At present, many studies have been conducted in this field around the world, including inter-radiometric calibration of different remote sensors (polar orbit and polar orbit, polar orbit and geostationary, geostationary and geostationary), on-site calibration based on a ground long-term stable target, e.g., the Libyan Desert [4–7] and Antarctic Dome C [8], and relying on the moon [9] for monitoring and radiometric calibration. The comprehensive use of the above methods has enabled the accuracy of satellite radiometric calibration to about 5%. Unfortunately, neither of these approaches can be applied uniformly across all operational satellites. Deep convective clouds are cold bright targets, which produce consistent albedos, making them ideal invariant Earth targets and well suited for calibration [12]. Hu *et al*. [13] and Doelling *et al*. [12] showed the possibility of the deep convective clouds (DCC) calibration technique and applied this technique to evaluate the stability of Visible and Infrared Scanner (VIRS), MODIS and AVHRR (Advanced Very High Resolution Radiometer) visible radiances onboard the Tropical Rainfall Measuring Mission (TRMM), Terra and NOAA satellites, respectively. Minnis *et al*. [14] further provide a spatial homogeneity threshold, and other selection

criteria, to reduce the occurrence. Fougnie and Bach [15] used the DCC method to calibrate Polarization and Directionality of the Earth Reflectances (POLDER) radiances. Doelling *et al*. [16] described in detail the characterization of DCC and showed that unlike stratus and cirrus clouds, the DCC spectra were not affected by water vapor absorption. Compared with desert targets and ice targets, DCC can provide more stable reflectance. Additionally, due to its larger sample size and fewer *a priori* data being required, it is better to apply this method to the re-calibration of the historical data of different satellites and to evaluate the accuracy of other calibration methods.

Table 1. Medium Resolution Spectral Imager (MERSI) spectral band specifications.

Band	Central Wavelength (μm)	Spectral Bandwidth (μm)	Resolution (m)	Noise	Dynamic Range
1	0.470	0.05	250	0.45	100
2	0.550	0.05	250	0.4	100
3	0.650	0.05	250	0.4	100
4	0.865	0.05	250	0.45	100
5	11.25	2.5	250	0.54 K	330 K
6	1.640	0.05	1,000	0.08	90
7	2.130	0.05	1,000	0.07	90
8	0.412	0.02	1,000	0.1	80
9	0.443	0.02	1,000	0.1	80
10	0.490	0.02	1,000	0.05	80
11	0.520	0.02	1,000	0.05	80
12	0.565	0.02	1,000	0.05	80
13	0.650	0.02	1,000	0.05	80
14	0.685	0.02	1,000	0.05	80
15	0.765	0.02	1,000	0.05	80
16	0.865	0.02	1,000	0.05	80
17	0.905	0.02	1,000	0.1	90
18	0.940	0.02	1,000	0.1	90
19	0.980	0.02	1,000	0.1	90
20	1.030	0.02	1,000	0.1	90

FY-3A, a Chinese second generation polar-orbit meteorological satellite, was launched on 27 May 2008. The local time at descending node is at 10:05, and the designed orbital maintenances are within 15 min·(2 yr)$^{-1}$. Medium Resolution Spectral Imager (MERSI) is a primary payload onboard FY-3A with 20 bands [17,18]. Since August 2008, when the satellite operationally provided science data, FY-3A/MERSI has been running on-orbit for over four years. Table 1 describes the band properties of FY-3A/MERSI. Band 5 is the infrared band with a center wavelength of 11.25 um. The remaining 19 bands are all RSBs, with the wavelength ranging from 412 nm to 2,130 nm. The design of the MERSI includes two experimental visible onboard calibration components: the visible onboard calibrator (VOC) and the space view (SV) [19]. The SV provides the dark signal. The VOC is the first experimental onboard visible calibration device for Fengyun series sensors. It is composed of three main optical components: a 6-cm diameter integrating mini-sphere, a beam expanding system and trap standard detectors [19]. It is used to monitor the radiometric response changes that arise either from the

MERSI degradation or a change in the VOC's output. However, because of the non-regular solar diffuser operation to avoid the solar diffuser's exposure to space, the VOC cannot get continuous data, and it has not worked since November 2011.

Dunhuang Radiometric Calibration Site in China has been the base for the VIS-NIR(Visible and Near Infrared) bands vicarious calibration for Chinese meteorological satellites for a long time [20]. However, in recent years, some new vicarious calibration methods have also been applied to the calibration and monitoring changes of sensors. Some preliminary results indicate that the annual update of calibration based on Dunhuang Calibration Site cannot monitor the degradation of a sensor in a satisfactory manner [21]. DCC-based radiometric calibration technology could be one of the ways to monitor long-term radiometric calibration for RSBs. Based on deep convective cloud targets, the long-term response changes of MERSI onboard FY-3A are derived.

2. Methodology

Deep convective clouds are extremely bright, cold, have large optical depths, are usually at the tropopause, have nearly a Lambertian reflectance and provide predictable albedos. On the RSBs, it can provide high and stable reflectance, which is suitable for calibration. Figure 1 shows the broadband albedo and reflectance (R) at 0.6 μm and 0.8 μm at the top of the atmosphere (Figure 1a), and the relative change rate ($dR/d\tau$) (Figure 1b) varies with cloud optical depth (COD, τ) from 1 to 1,000 by the Santa Barbara DISORT(Discrete Ordinates Radiative Transfer) Atmospheric Radiative Transfer (SBDART) [22] model. The relative change rate is the reflectance relative to the derivative of COD. The simulation condition is set to ocean, solar zenith angle 20 degrees, and the cloud optical depth varies from 1 to 1,000. It can be seen that the apparent reflectance increases with the increase of COD varying within 1–100. However, when the COD exceeds 100, the reflectance no longer changes with COD and tends to reach a stable value, and the relative change rate tends to be zero. The simulation result shows that DCC can be used as the invariant target for radiometric calibration. Furthermore, Figure 2 shows the apparent reflectance of top-of-atmosphere shortwave broadband changes with aerosol optical depth (AOD) under the same condition, as in Figure 1. The AOD of the troposphere is, respectively, 0.1, 0.2 and 0.5. It is found that the apparent reflectance is independent of the changes of aerosol and is mainly affected by cloud optical depth. The superiority of DCC over ground targets lies in the fact that most DCC is at the top of the troposphere, which can both minimize the impact of moisture and aerosol in the troposphere. It should be pointed out that most of the calibration targets are non-Lambertian reflectors and require a bidirectional reflectance distribution function (BRDF). Figure 3 presents the top-of-atmosphere apparent reflectance under the different conditions of solar zenith angle (SZA). It can be seen that the apparent reflectance of DCC is different with the angles, although it is smaller than 2%. This impact should not be ignored in the process of radiometric calibration.

Doelling *et al*. (2013) provides the baseline DCC technique used in the study. First, pixel level resolution (1 km) DCCs are identified by an infrared threshold [16]. As indicated by the results of vicarious infrared radiometric calibration researched by means of simultaneous observation in Qinghai Lake in 2008 and 2009, the brightness temperature observed through MERSI onboard calibration is systematically higher (the average value is 1.72 ± 1.18 °K) than that simulated by using site observed data. This phenomenon may result from the overestimated emissivity of the onboard blackbody. Thus,

the infrared threshold of deep convective clouds is set at 203.3°K to compensate for the overestimation of operational onboard MERSI brightness temperature.

Figure 1. (**a**) The broadband albedo and reflectance at 0.6 μm and 0.8 μm at TOA and (**b**) the relative ratio vary with cloud optical depth from 1 to 1,000 by Santa Barbara DISORT Atmospheric Radiative Transfer (SBDART) model simulation.

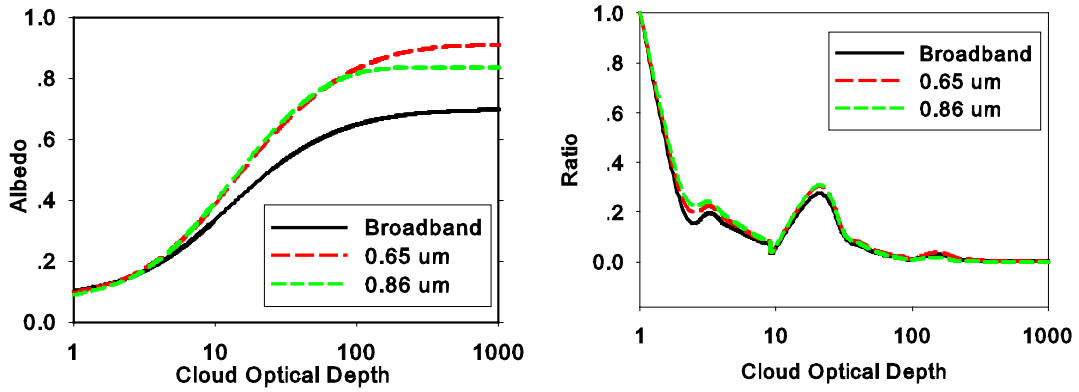

(**a**) (**b**)

Figure 2. SBDART simulated 0.6 μm and 0.8 μm TOA albedos as a function of cloud optical depth based on tropospheric aerosol optical depth inputs of 0.1, 0.2 and 0.5, respectively. The other parameters are the same as in Figure 1. AOD, aerosol optical depth.

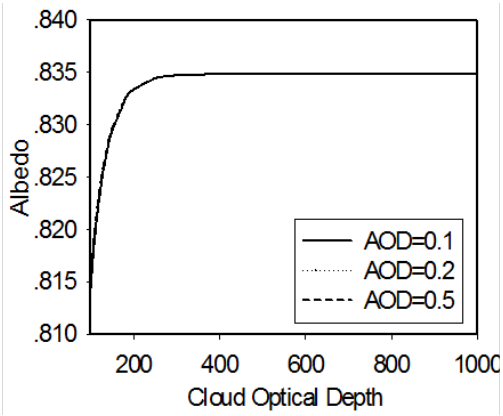

Figure 3. The reflectance at 0.*6* μm on TOA varies with cloud optical depth when solar zenith angles (SZA) are 10°, 20° and 30°, respectively.

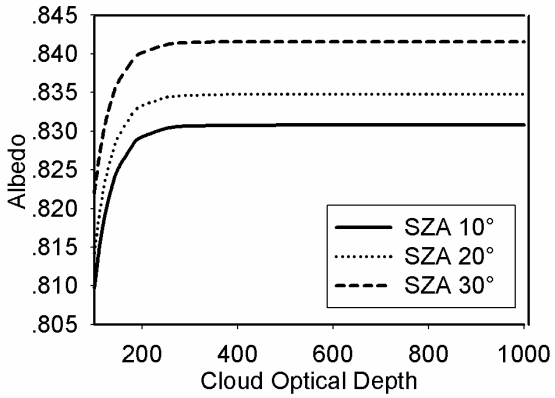

In order to reduce the amount of data and to avoid the effect of the inaccuracy of DCC BRDF with large solar zenith angle and satellite view zenith angle (VZA), data in the tropics oceans (15°N–15°S) and with solar zenith angle and satellite view zenith angle within 30° is used.

The calibration coefficient obtained from the pre-launch of FY-3A/MERSI is used to convert the Digital Number (DN) into the apparent reflectance for each band. The DCC bi-directional reflectance distribution function and the Earth-Sun distance need to be taken into account. The bi-directional reflectance model based on ice clouds with an optical thickness of 50° from the observation of CERES/TRMM (Clouds and Earth's Radiant Energy System/Tropical Rainfall Measuring Mission) is used to normalize the reflectance to a specified solar zenith angle. See Equation (1).

$$F(\theta_s) = \frac{\pi \quad L(\theta_s \quad ,\theta_v \quad ,\phi)}{R(\theta_s \quad , \quad \theta_v \quad , \quad \phi)} \tag{1}$$

where F is radiant flux density, L is radiance, θ_s is solar zenith angle, θ_v is satellite observation angle, ϕ is relative azimuth angle and R is the angular distribution model (ADM) based on CERES/TRMM observations.

To ensure that the uniform DCC targets are selected, spatial uniformity thresholds are also applied by computing the spatial standard deviation (σ) in the visible reflectance and IR of the identified pixel and its 24 adjacent neighbors (5 × 5 pixels). The selected DCC criteria are summarized as follows:

$$15°S < \text{Latitude} < 15°N,\ 5° < SZA < 30°,\ 0° < VZA < 30°$$

$$180K < IR < 203.3\ K,\ \sigma(IR) < 1\ K,\ \sigma(R) < 0.02,\ \text{Ocean only pixels}$$

Actually, monthly DCC reflectance value can be obtained by three kinds of methods (the averaged, median and peak mode of probability distribution function (mode), respectively). To assess the effect of ADM correction, Figure 4 shows the probability distribution functions (PDF) with different viewing angles before and after ADM correction by using monthly MERSI band 1 data. Here, the PDF bin is set as 0.01. The statistic values of different viewing angles for averaged, median and mode of PDF methods are shown in Table 2. A sunglint filter was applied, which is the cause of the reduced sampling of DCC pixels for view angles less than 20°. However, a sunglint filter is usually not applied in DCC calibration and is attributed to a coding oversight in this study. The sunglint filter does not alter the results of the DCC calibration.

Table 2. The probability distribution functions (PDF) mode, mean and median statistic as a function of the view angle of the MERSI band 1 deep convective clouds (DCC) pixel level reflectances for January 2012. "STD" refers to the standard deviation of the 4 view angle bin reflectances.

VZA	After ADM			Before ADM			Count Number
	Mode	Mean	Median	Mode	Mean	Median	
0–10	0.76	0.70	0.67	0.83	0.77	0.71	30144
11–20	0.76	0.71	0.67	0.84	0.79	0.72	256436
21–30	0.76	0.70	0.67	0.84	0.78	0.72	564305
31–40	0.75	0.70	0.66	0.83	0.76	0.70	540100
0–40	0.76	0.70	0.67	0.83	0.77	0.72	1390985
STD	0.0050	0.0050	0.0050	0.0058	0.0130	0.0096	

Figure 4. The probability distribution functions of MERSI band 1 DCC pixel level reflectances as a function of viewing angle before (**a**) and after (**b**) angular distribution model (ADM) correction for January 2012.

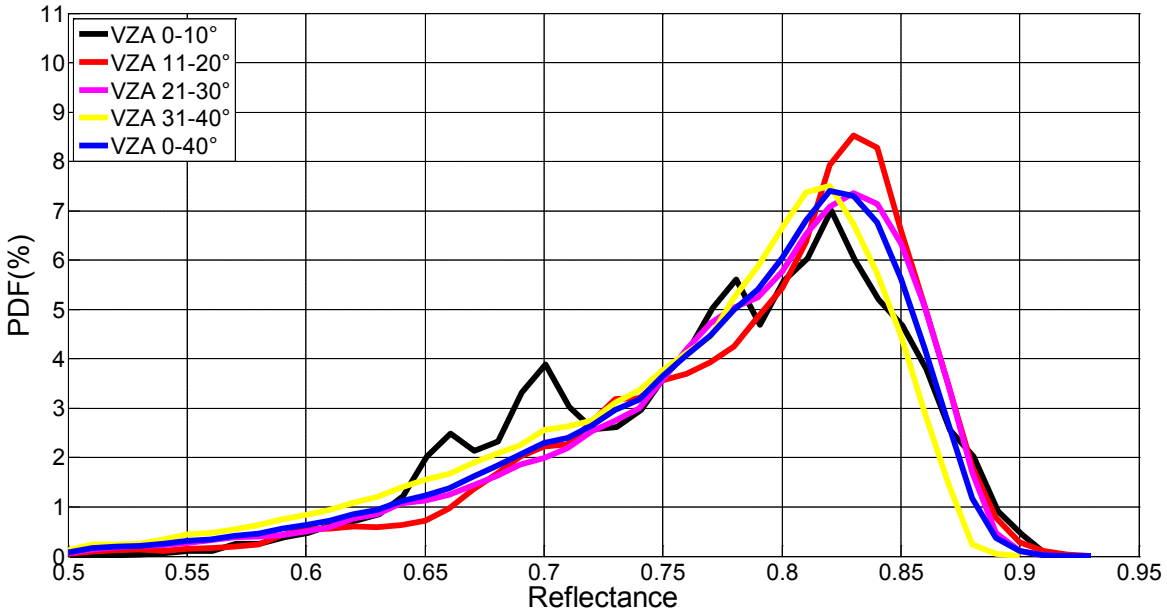

(**a**)

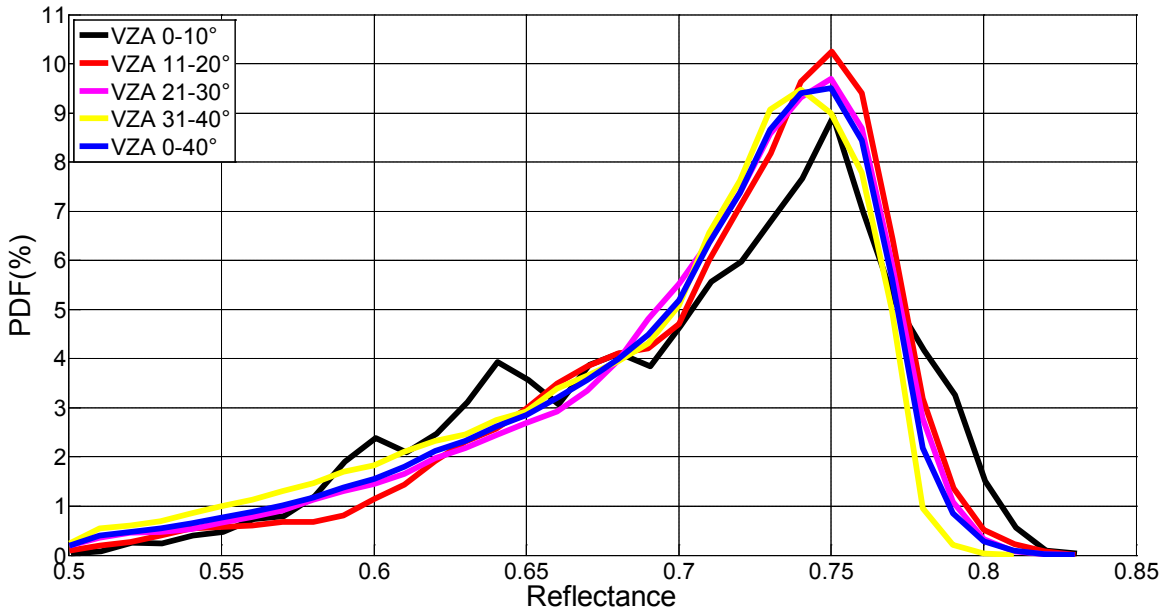

(**b**)

It is quite different before and after ADM correction for the three kinds of methods. The PDF DCC reflectance statistics as a function of view angle are obviously more consistent after ADM correction. The standard deviation of reflectances on various viewing angles for three methods all decrease after correction. The mode statistic also provides the most consistent view angle reflectance without the application of an ADM correction.

The DCC samples are selected from among all data for the global low-latitude ocean. Despite a series of screenings, including angle limiting, during a month, there are at least tens of thousands of valid samples, providing adequate sources for sample selection.

3. Results and Analysis

3.1. The Degradation of FY-3A/MERSI by DCC Method

DCC reflectance data are used to monitor the sensor response of 19 RSB bands of FY-3A/MERSI during the period from August 2008, to August 2012. The monthly PDF mean, median and mode of the DCC reflectance are regressed separately to provide the degradation rate of the MERSI visible bands using a quadratic fit. Additionally, the total degradations are derived from quadratic curve fitting. The total degradations of each RSB (except band 6 and 7) since August 2008, for three methods are listed in Table 3. Besides evaluating the degradation of each band, uncertainty for each method is also evaluated by a normalized index (2σ/mean). Here, σ represents the standard error or standard deviation of the residuals about the quadratic fit, and the mean is the averaged value of the estimation from the fitting model. A smaller 2σ/mean indicates a lower dispersion degree of the target and a higher stability of the method.

Table 3. Total degradation of the FY-3A/MERSI bands based on a quadratic regression of the PDF mean, median and mode statistic of monthly DCC reflectances during August 2008, and August 2012.

	Bands	Central Wavelength	Mean %	Median %	Mode %	2σ/Mean % Mean	2σ/Mean % Median	2σ/Mean % Mode
Blue	8	412	37.84	37.63	38.02	2.89	2.73	2.42
	9	443	20.88	21.00	21.85	2.10	2.17	2.63
	1	470	14.42	14.52	14.93	2.01	2.12	2.09
	10	490	11.38	11.51	12.3	1.87	1.93	2.28
Vis-NIR	11	520	2.60	2.44	2.05	2.20	2.08	2.09
	2	550 (250 m)	5.79	5.90	6.85	1.82	1.95	1.94
	12	565	2.47	2.61	3.26	1.69	1.81	2.25
	3	650 (250 m)	−2.45	−2.19	−1.42	1.88	1.99	1.70
	13	650	−1.88	−1.57	−0.5	1.88	1.88	1.88
	14	685	−1.60	−1.31	−0.41	1.87	1.89	2.15
	4	765	0.49	1.18	1.21	1.83	1.56	1.74
	16	865 (250 m)	−0.20	0.35	0.15	2.11	1.57	2.42
	15	865	1.60	1.91	2.7	2.06	2.12	2.71
	20	1030	15.87	15.86	15.91	1.41	1.46	1.78
WV	17	905	5.85	5.98	6.02	2.01	1.41	1.41
	18	940	9.05	9.04	9.4	1.84	1.97	2.39
	19	980	7.84	8.49	8.81	1.22	1.26	1.52

The results show that the total degradations of FY-3A/MERSI by three kinds of monthly DCC statistics methods are quite consistent. These three methods are monthly mean, monthly medium value and monthly PDF mode. The differences in total degradations are no more than 1% among the three methods. The 2σ/mean indexes of all bands are less than 3%, and most indexes of bands are less than 2%. Especially the indexes in the three water vapor absorption bands are under 2%. These absorption bands (bands 17–19) are often difficult to handle by the traditional vicarious radiometric calibration method, such as site vicarious calibration. However, the DCC spectra are nearly not affected by water vapor absorption, since little water vapor is above the DCC.

Figure 5 shows the monthly mean DCC-based MERSI response change for 19 bands, respectively. According to the response change characteristics, the 19 bands can be divided into four groups: the blue bands group with the center wavelength shorter than 500 nm (Figure 5a), the visible and near-infrared band group (Figure 5b), the water vapor bands group (Figure 5c) and the shortwave infrared group (Figure 5d). The long-term sensor often varies with the time series. In order to analyze this variation, we perform linear fitting on the annual degradation rate and linear and quadratic curve fitting on the total degradation, respectively.

Figure 5. The monthly mean DCC-based MERSI response change for 19 bands, respectively, during the period from August, 2008, to August, 2012. (**a**) Blue bands; (**b**) near-infrared bands; (**c**) water-vapor bands; (**d**) short-wave bands.

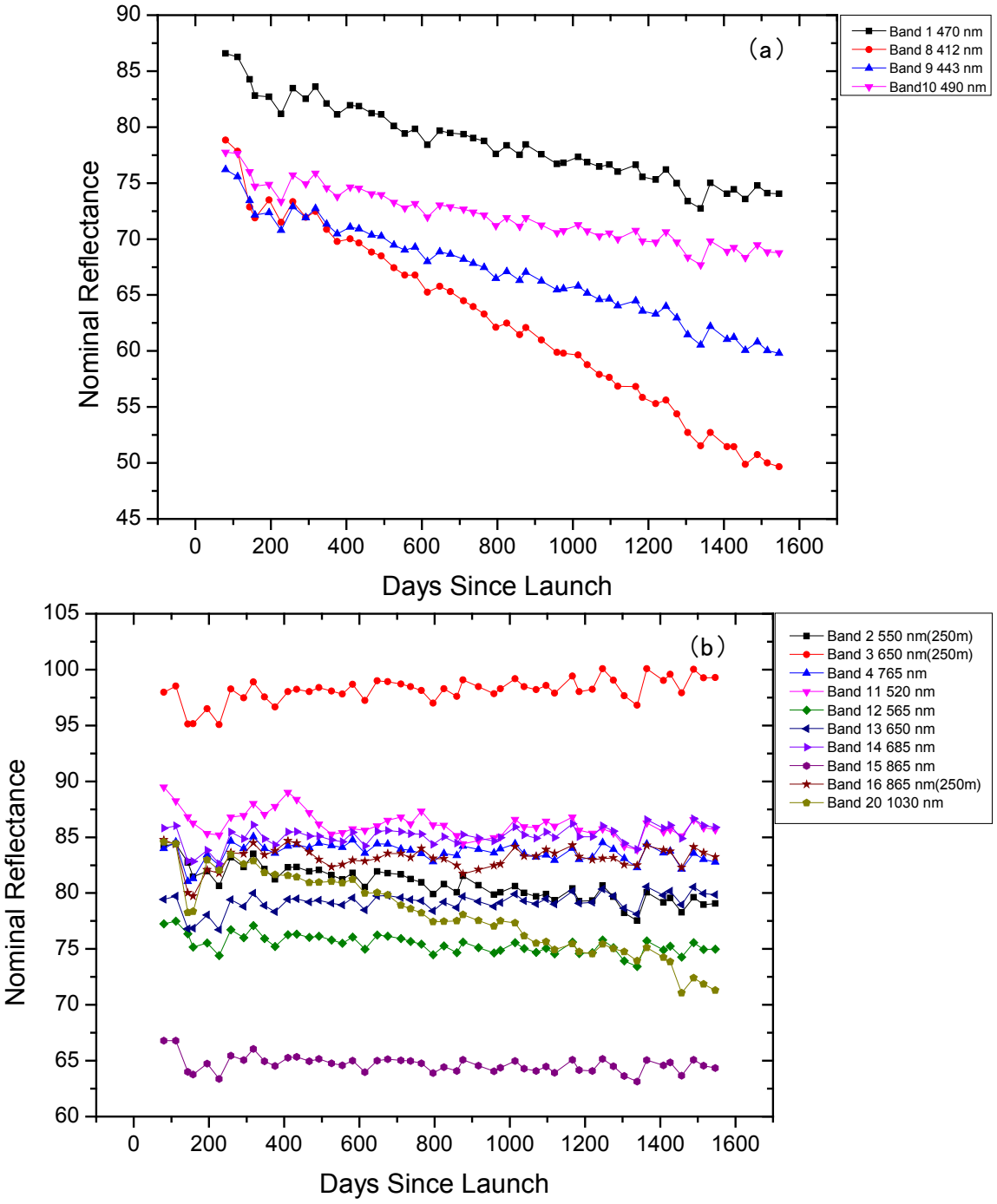

Figure 5. *Cont.*

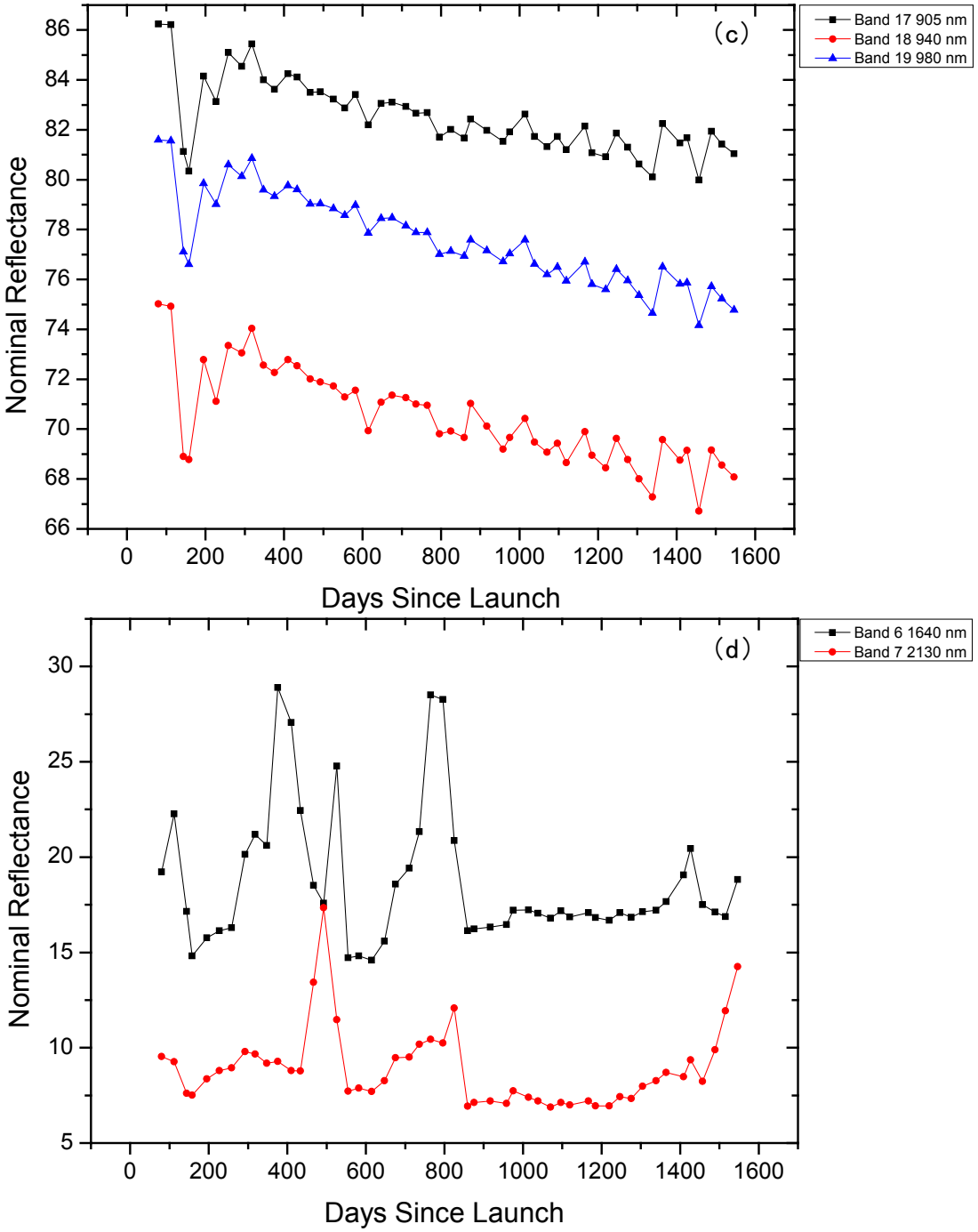

Table 4 lists the annual degradation rate by linear fitting, as well as the total degradation by linear and quadratic fitting.

The four blue bands show the greatest degradation. The total degradations of each blue band are all larger than 10%. The largest degradation is 37.84% for the 412 nm band. Meanwhile the 490 nm band shows the smallest degradation of this group, decreasing by 11.4%. Moreover, the shorter the band center wavelength, the more serious the degradation is. This wavelength-dependent response change is also found in MODIS [23,24]. The MERSI blue band annual degradation rates are largest in the first year and then taper off (see Table 4). After that, the rates seem to become larger in recent years (August 2011–August 2012).

Table 4. Degradation rates (% per time period) for the FY-3A/MERSI bands using the DCC mean method.

	Bands	Central Wavelength	8–9 August Linear Fit	9–10 August Linear Fit	10–11 August Linear Fit	11–12 August Linear Fit	8–12 August Linear Fit	8–12 August Quadratic Fit	2σ/Mean % Linear	2σ/Mean % Quadratic
Blue	8	412	9.99	8.54	8.03	9.26	37.89	37.84	2.89	2.89
	9	443	6.34	4.55	4.04	5.80	20.89	20.88	2.10	2.10
	1	470	5.25	3.47	2.44	2.48	14.54	14.42	2.26	2.01
	10	490	3.82	2.88	2.05	2.02	11.44	11.38	2.02	1.87
Vis-NIR	11	520	−0.42	0.40	−0.91	−0.04	2.58	2.60	2.25	2.20
	2	550 (250 m)	1.97	1.12	1.22	1.08	5.79	5.79	1.83	1.82
	12	565	1.5	1.07	0.64	0.11	0.07	2.47	2.48	1.69
	3	650 (250 m)	−1.19	−0.50	−0.73	−0.62	−2.42	−2.45	1.90	1.88
	13	650	−1.30	−0.33	−0.67	−0.59	−1.86	−1.88	1.89	1.88
	14	685	−0.94	−0.41	−0.84	−0.76	−1.60	−1.60	1.87	1.87
	4	765	−1.91	0.73	0.04	0.73	0.54	0.49	1.95	1.83
	16	865 (250 m)	−1.61	−0.09	−1.57	−0.25	−0.22	−0.20	2.11	2.11
	15	865	0.96	0.32	0.060	−0.08	1.58	1.60	2.09	2.06
	20	1,030	3.78	4	3.28	4.20	15.87	15.87	1.68	1.41
WV	17	905	2.50	1.41	0.57	0.16	5.69	5.85	2.18	2.01
	18	940	3.06	1.99	1.57	1.24	8.94	9.05	1.84	1.84
	19	980	0.90	2.02	1.32	1.29	7.84	7.84	1.59	1.59

The visible and near infrared (Vis-NIR) bands with the center wavelength longer than 500 nm are relatively stable, with a less than 3% response change, except for bands 2 (550 nm, 250 m spatial resolution) and 20 (1,030 nm). The 765 and 865 nm bands are the most stable bands, with the total changes standing at 0.49 and−0.2%, respectively. Different from the blue bands, whose response decreases rapidly, the responses for the 650 nm, 685 nm and 865 nm bands show a little bit of an increase. The result of the 650 nm band shows the largest increase of the response, reaching to about 2.45%. This conclusion agrees with the analysis of visible-NIR onboard calibrator (VOC) [19]. However for band 20 (1,030 nm), there is a total of a 15.87% decrease.

These three water-vapor(WV) bands, with wavelengths at 905 nm, 940 nm and 980 nm, show obvious degradation, all exceeding 5%. The 940 nm water vapor absorption band at the absorption peak shows the largest degradation, reaching 9.05%. The annual degradation rates of 905 nm and 940 nm bands also reduce gradually. About three months after the satellite launched (October 2008), there was an abnormal drop in these water-vapor bands. These phenomena also can be found in other bands, although not as clearly as in the water-vapor bands. The reason is an adjustment had been done to the instrument on board from 13 to 28 November. This adjustment stopped the onboard processing of detector difference normalization for image de-striping. Monthly mean DCC has the ability to monitor the abnormal state on board. These abnormal DCC data had been excluded when we calculated degradation and the 2σ/mean index.

For shortwave infrared band 6 and 7 (1,640 nm and 2,130 nm), a smooth trend fitting is unavailable. DCC reflectance shows an abnormal jump, which is more significant in band 6 than in band 7. This jump

is no longer observed, after 900 days of the satellite launch (after November 2010). It had remained stable for one and a half years. However, this jump began to appear again in March 2012. Figure 6 shows the results of the space view (SV) of MERSI bands 6 and 7. The results indicate that an abnormal jump did occur to cold space in bands 6 and 7 at the same time. The shortwave infrared bands 6 and 7 of MERSI have been designed as an adjustable electronic gain under telemetry control when the signal responses of these two bands become small. However, the outer space environment influence on the instrument caused the random jump in the electronic gain without the gain adjustment maneuver. This is the reason why it is impossible to obtain an effective response change curve by DCC. After December 2010, the onboard electric gain seemed to be locked. It is also shown that DCC reflectance became stable without any abnormal jump when the electric gain was stable.

Figure 6. Space view (SV) Digital Number (DN) of FY-3A/MERSI bands 6 and 7 from July 2008 to April 2013.

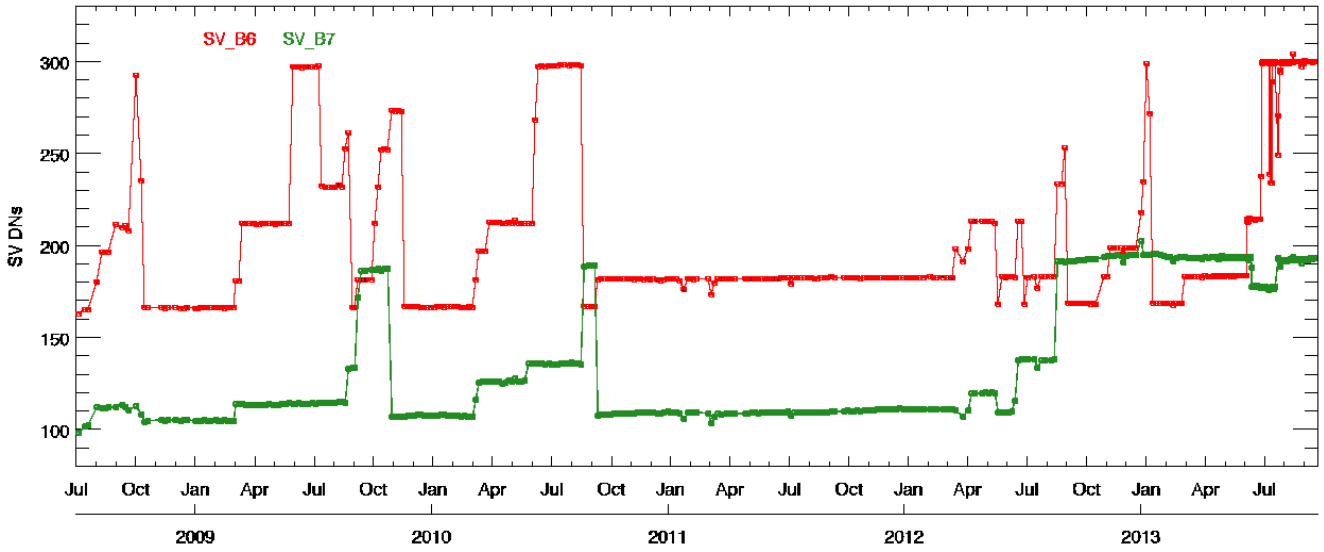

For most bands with total degradation over 5%, the annual degradation rate is decreasing yearly. Especially in the first year after the satellite was launched, the bands degraded fastest. The total degradation rate obtained by linear fitting and quadratic curve fitting differs by less than 0.3%, because in recent years, the annual degradation rate sped up.

The 2σ/mean indexes of all bands are less than 2.5%, excluding band 8 with 2.89%. The index is below 2% in the three water vapor absorption bands, which are difficult to properly handle by the traditional vicarious radiometric calibration method. The 2σ/mean index is very small, indicating the stability and reliability of the DCC-based radiometric calibration and monitoring method. The smaller index from quadratic fitting than that from linear fitting reveals that the quadratic fit curve can better describe the degradation characteristics of the data.

3.2. Comparison with Other Methods

A well-calibrated satellite sensor can inter-calibrate another satellite sensor with inferior calibration by comparing coincident co-located measurements. The keys to inter-calibration are the consistency of two sensors' spectral response functions, the consistency of the observation target geometry, as well as

the uniformity and stability of the observation target. The MODIS instrument has an excellent onboard calibration system with an absolute calibration accuracy of 2% [23,24]. Using Aqua/MODIS collection 5 data in August 2008, and August 2012, as the reflectance reference, we do Simultaneous Nadir Overpass (SNO) inter-calibration for the similar bands between Aqua/MODIS and FY-3A/MERSI (MERSI bands 1, 2, 3, 8, 10, 12, 13 and 15). The differences of the spectral response function (SRF) between MERSI and MODIS are not considered here. The spatial and temporal collocated satellite pairs with similar viewing geometry are essential to the success of instrument inter-calibration. Collection 5 products of MODIS L1 data are selected when the nadirs of the two satellites overpass the same target within 5 min. The measurements are projected onto the same region of 1,024 × 1,024 in 1-km resolution viewing geometry collocation is performed using three criteria:

$$VZA < 35°, SZA < 80°, |\cos(VZA_{MODIS})/\cos(VZA_{MERSI}) - 1| < 0.01$$

As for the differences in the SRF, only MERSI bands 1, 2, 3, 8, 10, 12, 13 and 15, whose SRF is similar to MODIS bands, are considered here. Using this calibration efficiency of August 2008, and August 2012, the linear degradations of MERSI bands 1, 2, 3, 8, 10, 12, 13 and 15 are calculated during this period.

To increase the in-flight calibration frequency, a multisite radiometric calibration monitoring method is presented by Sun *et al*. [21]. This method relies on simulated radiances over several Committee on Earth Observation Satellites (CEOS)/WGMS recommended invariant earth targets, which include Libya-1, Libya-4, Arabia-2 and Dunhuang, as well as a clear-sky pristine dark ocean site at Lanai. The calibration gain is based on a linear regression using all available measurements from all five sites every 10 days. This method is referred to as the multi-site method in this paper. The annual degradation rates by the multi-site method are from [21]. The total degradations for four years are adjusted for the period of August 2008 to August 2012, by annual degradation rates.

Since 2002, vicarious calibration based on the Dunhuang Radiometric Calibration Site became the operational calibration method for the Fengyun satellites [19,20]. The Dunhuang site was selected in 2008 by the Working Group on Calibration and Validation (WGCV) of the Committee on Earth Observation Satellites (CEOS) as one of the instrumented reference sites. The annual CRCS field campaign for MERSI VC has been conducted based on synchronous satellite-ground measurements since September 2008. Because of the huge resources, CRCS vicarious calibration can be conducted only once a year. The 2008 to 2011 CRCS VC results come from [21], and the results of 2012 come from the CRCS 2012 technology report. The total degradations for four years are also adjusted for the same period.

Comparisons of these four methods for total degradation of FY-3A/MERSI are summarized in Table 5. For most bands, there is good consistency of the total degradation with a maximum bias less than 3%, except for bands 11, 18 and 19. The bias between DCC and the other three methods of band 11 is up to 7.71%. Obviously, compared with the other three methods, the degradation from the DCC method for band 11 is underestimated. The reason is that DCC reflectance in band 11 of FY-3A/MERSI is saturated. The DCC nominal reflectance of band 11 is about from 80% to 90%. Doelling *et al*. (2013) [16] show that the DCC reflectance is about 90% at 520 nm with SCIAMACHY (Scanning Imaging Absorption Spectrometer for Atmospheric Chartography) hyper-spectral observation. However, according to Table 1, the dynamic range of band 11 is no more than 80%. The same situation can also be found in

bands 14 and 16. Fortunately, these two bands do not show apparent degradation, while band 11 has an obvious response change. Figure 7 shows the PDF of MERSI band 11 (Figure 7a), band 14 (Figure 7b) and band 16 (Figure 7c) of DN for August 2008 to August 2012. The maximum MERSI DN is 4,096. The peaks of DN PDF for these three bands are saturated. The percentages of saturated pixels are reducing gradually for bands 11 and 16 as time goes by, but saturation is still a big issue. Compared with bands 11 and 16, the saturated pixels for band 14 are relative few. The greatest frequency of pixels DN is between 3,500 and 4,000. The second largest bias is in band 18 (940 nm), the strong water vapor absorption band. Although the Dunhuang Site and Multisite methods show much bigger degradation than the DCC method, the uncertainty of these two methods are much bigger than DCC [21]. The uncertainty is related to the accuracy of water vapor measurement and radiative transfer model simulation, especially in the strong water absorption band. The simulated radiances in the water vapor bands can be quite variable and highly dependent on the water vapor amount from either an assimilated dataset or GCM, giving rise to large uncertainties. This will cause an absolute calibration difference. The DCC spectra is slightly affected by water vapor absorption, since there is little water vapor above the top of the troposphere. The 2σ/mean uncertainties are much smaller than other methods. However, it should be noted that the variation of water vapor in the stratosphere could be the source of error in water vapor bands by the DCC method.

Table 5. Total degradations of FY-3A/MERSI from August 2008 to August 2012, for four methods.

	Bands	Central Wavelength	DCC (%)	Aqua-MODIS SNO (%)	Dunhuang Site (%)	Multi-Site (%)	Mean (except DCC, %)	Bias (DCC-Mean, %)	STD
Blue	8	412	37.84	35.43	36.76	38.08	36.76	1.08	1.21
	9	443	20.88	NA	20.65	23.94	22.30	−1.42	1.84
	1	470	14.42	15.99	14.44	18.18	16.20	−1.78	1.77
	10	490	11.38	13.18	10.74	15.67	13.20	−1.82	2.21
Vis-NIR	11	520	2.60	NA	8.57	12.04	10.31	−7.71	4.77
	2	550 (250 m)	5.79	6.58	5.67	9.12	7.12	−1.33	1.60
	12	565	2.47	4.67	3.75	6.00	4.81	−2.34	1.49
	3	650 (250 m)	−2.45	−1.25	0.83	−2.46	−0.96	−1.49	1.55
	13	650	−1.88	−3.2	0.45	−1.32	−1.36	−0.52	1.51
	14	685	−1.60	NA	1.43	−1.59	−0.08	−1.52	1.75
	15	765	0.49	−2.76	1.79	1.81	0.28	0.21	2.15
	4	865 (250 m)	−0.20	NA	2.14	−0.31	0.92	−1.12	1.38
	16	865	1.60	NA	3.81	1.21	2.51	−0.91	1.40
	20	1,030	15.87	NA	17.33	16.06	16.70	−0.83	0.79
WV	17	905	5.85	NA	4.00	7.13	5.57	0.29	1.57
	18	940	9.05	NA	16.00	14.52	15.26	−6.21	3.66
	19	980	7.84	NA	11.92	10.18	11.05	−3.21	2.05

Figure 7. Probability distribution functions of MERSI band 11 (**a**), band 14 (**b**) and band 16 (**c**) of DN for August 2008 to August 2012.

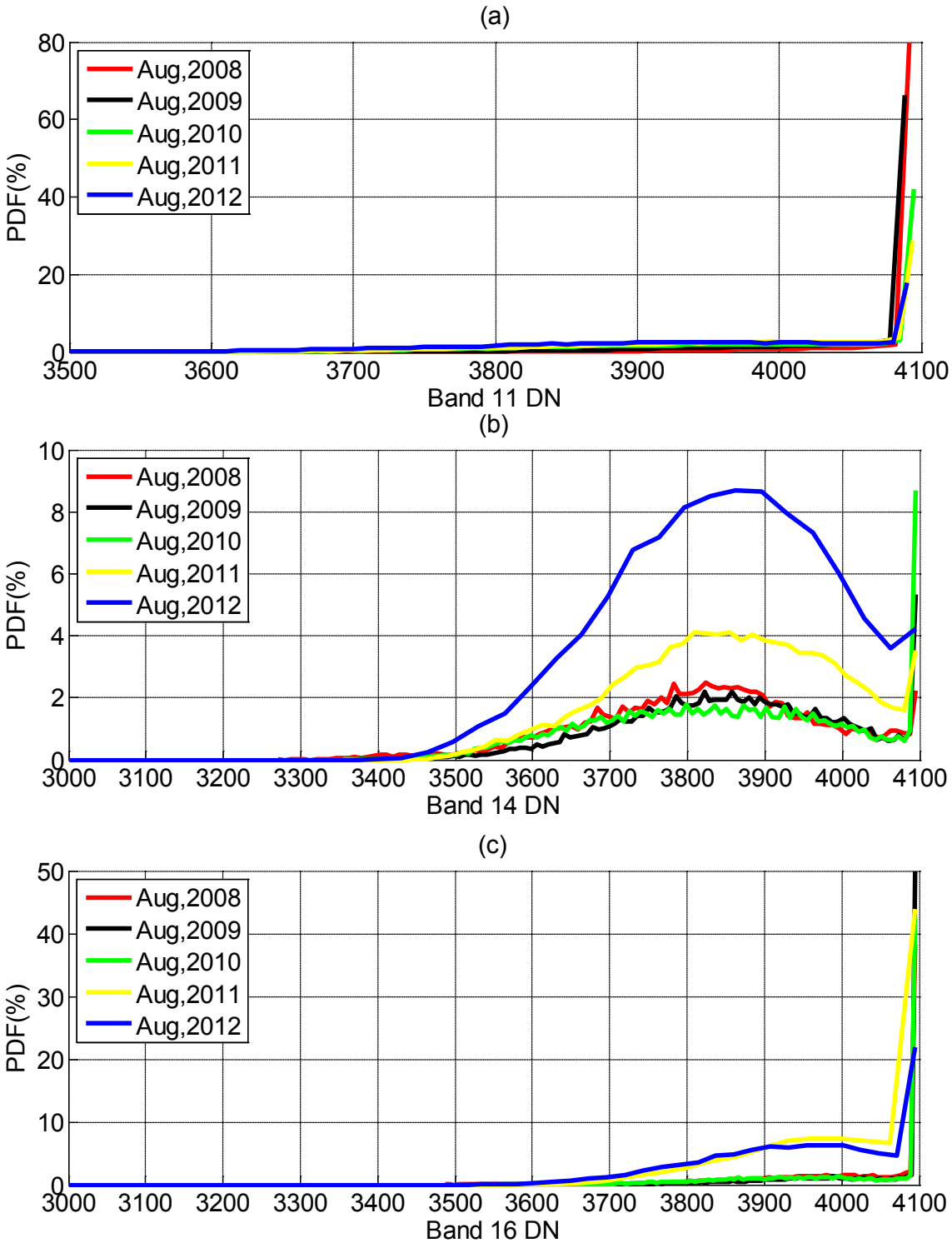

4. Conclusions

The radiative transfer simulation results show that the DCC reflectances are stable for cloud optical depths greater than 200 and also independent of tropospheric aerosol optical depth. Therefore, DCC

targets are used to monitor the long-term response change of all 19 RSBs of FY-3A/MERSI, and these results are compared with the other three calibration methods.

The results of calibration monitoring for FY-3A/MERSI show: (1) Not only can the long-term radiometric response trend of MERSI RSBs be well illustrated by the DCC method, but also instrument anomalies can also be detected by DCC. The abnormal gain jump in bands 6 and 7 on orbit can be seen in the results. (2) Blue bands whose center wavelength is shorter than 500 nm and water-vapor absorption bands show obvious degradation. The total degradations of band 8 (412 nm) is up to 37.4% during the past four years. The degradations of three water vapor absorption bands are more than 5%. By contrast, the degradations of the near-infrared bands are less than 3%, except bands 3 and 20, and even some bands illustrate a little increase of the radiometric response. (3) The degradation rates are greatest during the first year in orbit and decreases over time. However, for some bands, there was an increase in the degradation rate during the last year. (4) The DCC degradation uncertainty (2σ/mean) is within 2.5%, except band 8, using the mean method.

The degradation results derived from DCC monitoring are consistent with the other methods, including Aqua/MODIS SNO inter-calibration, the multisite method and the Dunhuang site vicarious calibration. The largest difference of degradation between DCC and others is less than 3%, except for bands 11, 18 and 19. Due to the limit of dynamic range, the DCC method is not suitable for monitoring the response change of bands 11, 14 and 16. As noted, for the NIR water vapor bands, which are difficult to calibrate using invariant Earth surface targets, the DCC degradation uncertainty was less than 2%. The multi-site method and Dunhuang vicarious calibration uncertainties are much greater than that from DCC calibration [21], which demonstrates a significant advantage for using DCC calibration for these bands.

The FY-3A/MERSI DCC calibration method described in this paper is not an absolute calibration method, but relative calibration trend monitoring. In fact, DCC is a relatively bright and stable target, and its TOA apparent reflectance can be obtained or simulated in advance. DCC's reflectance could be obtained by either radiative model simulation [25,26] or a reference sensor, such as MODIS or SCIAMACHY [16]. Therefore, absolute vicarious calibration-based DCC will be possible in the future, if we can have a good DCC reflectance model. Moreover, the DCC method does not need additional auxiliary data and is more suitable for the recalibration of historical satellite data. This is a promising calibration method for the re-calibration of Chinese first generation satellites, FY-1C/1D.

Acknowledgments

This paper is supported by the foundation of "The National Key Basic Research and Development Plan (973 Project) (Grant No. 2010CB950802, and 2011CB403401)" and the "National Natural Science Foundation of China (Grant No. 41105010)". We are grateful to the anonymous reviewers for their insightful comments.

Conflicts of Interest

The authors declare no conflict of interest.

References

1. Dinguirard, M.; Slater, P.N. Calibration of space multispectral imaging sensor: A review. *Remote Sens. Environ.* **1999**, *68*, 194–205.
2. Hu, X.Q.; Zhang, Y.X.; Qiu, K.M. In-flight radiometric calibration for VNIR channels of FY-1C satellite sensor by using irradiance based method (In Chinese). *J. Remote Sens.* **2003**, *7*, 458–464.
3. Xiong, X.; Barnes, W. An overview of MODIS radiometric calibration and characterization. *Adv. Atmos. Sci.* **2006**, *23*, 69–79.
4. Rao, C.R.N.; Chen, J. Inter-satellite calibration linkages for the visible and near-infrared channels of the Advanced Very High Resolution Radiometer on the NOAA-7, -9, and -11 spacecraft. *Int. J. Remote Sens.* **1995**, *16*, 1931–1942.
5. Koslowsky, D. Signal degradation of the AVHRR shortwave channels of NOAA 11 and NOAA 14 by daily monitoring of desert targets. *Adv. Space Res.* **1997**, *19*, 1355–1358.
6. Minnis, P.; Nguyen, L.D.; Doelling, D.R.; Young, D.F.; Miller, W.F.; Kratz, D.P. Rapid calibration of operational and research meteorological satellite imagers. *J. Atmos. Oceanic Ocean. Technol.* **2002**, *19*, 1233–1249.
7. Heidinger, A.K. Calibration of visible and near-infrared channels of the NOAA-12 AVHRR using time series of observations over deserts. *Int. J. Remote Sens.* **2003**, *24*, 3635–3649.
8. Six, D.; Fily, M.; Alvain, S.; Henryc, P.; Benoist, J.P. Surface characterisation of the Dome Dome Concordia area (Antarctica) as a potential satellite calibration site, using Spot 4/Vegetation instrument. *Remote Sens. Environ.* **2004**, *89*, 83–94
9. Eplee, R.E.; Barnes, R.A.; Patt, F.S.; Meister, G.; McClain, C.R. SeaWiFS Lunar Calibration Methodology after Six Years on Orbit. In Proceedings of Earth Observing Systems IX, Denver, CO, USA, 26 October 2004.
10. Mitchell, D.G. Global Space-Based Inter-Calibration System (GSICS). *Proc. SPIE* **2007**, *6684*, doi:10.1117/12.735246.
11. Goldberg, M.; Ohring, G.; Butler, J.; Cao, C.; Datla, R.; Doelling, D.V.; Hewison, G.T.; Iacovazzi B.; Kim, D.; Kurino, T.; *et al*. The global space-based inter-calibration system. *Bull. Am. Meteorol. Soc.* **2011**, *92*, 467–475.
12. Doelling, D.R.; Nguyenb, L.; Minis, P. On the Use of Deep Convective Clouds to Calibrate AVHRR Data. In Proceedings of Earth Observing System IX, Denver, CO, USA, 26 October 2004.
13. Hu, Y.; Wielicki, B.A.; Yang, P.; Stackhouse, P.W.; Lin, B.; Young, D.F. Application of deep convective cloud albedo observation to satellite-based study of the terrestrial atmosphere: Monitoring the stability of spaceborne measurements and assessing absorption anomaly. *IEEE Trans. Geosci. Remote Sens.* **2004**, *42*, 2594–2599.
14. Minnis, P.; Doelling, D.R.; Nguyen, L. Assessment of the visible channel calibrations of the VIRS on TRMM and MODIS on Aqua and Terra. *J. Atmos. Ocean. Technol.* **2008**, *25*, 385–400.
15. Fougnie, B.; Bach, R. Monitoring of radiometric sensitivity changes of space sensors using deep convective clouds: Operational application to PARASOL. *IEEE Trans. Geosci. Remote Sens.* **2009**, *47*, 851–861.

16. Doelling, D.R.; Daniel, M.; Benjamin, R.S.; Rajendra, B.; Arun, G. The characterization of deep convective clouds as an invariant calibration target and as a visible calibration technique. *IEEE Trans. Geosci. Remote Sens.* **2013**, *51*, 1147–1159.
17. Yang, J.; Dong, C.H.; Lu, N.M. FY-3A: The new polar-orbiting meteorological satellite of China. *Acta Meteorol. Sin.* **2009**, *67*, 0501–0509.
18. Dong, C.; Yang, J.; Zhang, W.; Yang, Z.; Lu, N.; Shi, J.; Zhang, P.; Liu, Y.; Cai, B. An overview of a new Chinese weather satellite FY-3A. *Bull. Am. Meteorol. Soc.* **2009**, *90*, 1531–1544.
19. Hu, X.Q.; Sun, L.; Liu, J.J.; Ding, L.; Wang, X.; Li, Y.; Zheng, Z.J.; Xu, N.; Chen, L. Calibration for the solar reflective bands of medium resolution spectral imager onboard FY-3A. *IEEE Trans. Geosci. Remote Sens.* **2012**, *50*, 4915–4928.
20. Hu, X.Q.; Liu, J.J.; Sun, L.; Rong, Z.G.; Li, Y.; Zhang, Y.; Zheng,Z.; Wu,R.; Zhang,L.; Gu, X. Characterization of CRCS Dunhuang test site and vicarious calibration utilization for Fengyun (FY) series sensors. *Can. J. Remote Sens.* **2010**, *36*, 566–582.
21. Sun, L.; Hu, X.Q.; Guo, M.H.; Xu, N. Multi-site calibration tracking for FY-3A mersi solar bands. *IEEE Trans. Geosci. Remote Sens.* **2013**, *50*, 4929–4942.
22. Ricchiazzi, P.; Yang, S.; Gautier, C.; Sowle, D. SBDART: A research and teaching software tool for plane-parallel radiative transfer in the Earth's atmosphere. *Bull. Am. Meteorol. Soc.* **1998**, *79*, 2101–2114.
23. Xiong, X.; Sun, J.; Barnes, W.; Salomonson, V.; Esposito, J.; Erives, H.; Guenther, B. Multiyear on-orbit calibration and performance of Terra MODIS solar reflective bands. *IEEE Trans. Geosci. Remote Sens.* **2007**, *45*, 879–889.
24. Xiong, X.; Sun, J.; Xie, X.; Barnes, W.L.; Salomonson, V.V. On-orbit calibration and performance of Aqua MODIS reflective solar bands. *IEEE Trans. Geosci. Remote Sens.* **2010**, *48*, 535–546.
25. Sohn, B.J.; Ham, S.H.; Han, Y. Possibility of the visible-channel calibration using deep convective clouds overshooting the TTL. *J. Appl. Meteorol. Climatol.* **2009**, *48*, 2272–2283.
26. Sterckx, S.; Stefan L.; Stefan A. Rayleigh, deep convective clouds, and cross-sensor desert vicarious calibration validation for the PROBA-V mission. *IEEE Trans. Geosci. Remote Sens.* **2013**, *51*, 1437–1452.